NANO LETTERS
Letter
pubs.acs.org/NanoLett

Hydrogen-Induced Morphotropic Phase Transformation of Single-Crystalline Vanadium Dioxide Nanobeams

Woong-Ki Hong,[*,†,‡,□] Jong Bae Park,[‡,□] Jongwon Yoon,[§] Bong-Joong Kim,[*,§] Jung Inn Sohn,[†,¶] Young Boo Lee,[‡] Tae-Sung Bae,[‡] Sung-Jin Chang,[∥] Yun Suk Huh,[∥] Byoungchul Son,[‡] Eric A. Stach,[⊥] Takhee Lee,[*,#] and Mark E. Welland[†]

[†]Nanoscience Centre, University of Cambridge, Cambridge CB3 0FF, United Kingdom
[‡]Jeonju Center, Korea Basic Sicence Intstitute, Jeonju, Jeollabuk-do 561-180, Korea
[§]School of Material Science and Engineering, Gwangju Institute of Science and Technology, Gwangju 500-712, Korea
[∥]Division of Material Science, Korea Basic Science Institute, Daejoen 305-333, Korea
[⊥]Center for Functional Nanomaterials, Brookhaven National Laboratory, Upton, New York 11973, United States
[#]Department of Physics and Astronomy, Seoul National University, Seoul 151-744, Korea

Supporting Information

ABSTRACT: We report a morphotropic phase transformation in vanadium dioxide (VO_2) nanobeams annealed in a high-pressure hydrogen gas, which leads to the stabilization of metallic phases. Structural analyses show that the annealed VO_2 nanobeams are hexagonal-close-packed structures with roughened surfaces at room temperature, unlike as-grown VO_2 nanobeams with the monoclinic structure and with clean surfaces. Quantitative chemical examination reveals that the hydrogen significantly reduces oxygen in the nanobeams with characteristic nonlinear reduction kinetics which depend on the annealing time. Surprisingly, the work function and the electrical resistance of the reduced nanobeams follow a similar trend to the compositional variation due mainly to the oxygen-deficiency-related defects formed at the roughened surfaces. The electronic transport characteristics indicate that the reduced nanobeams are metallic over a large range of temperatures (room temperature to 383 K). Our results demonstrate the interplay between oxygen deficiency and structural/electronic phase transitions, with implications for engineering electronic properties in vanadium oxide systems.

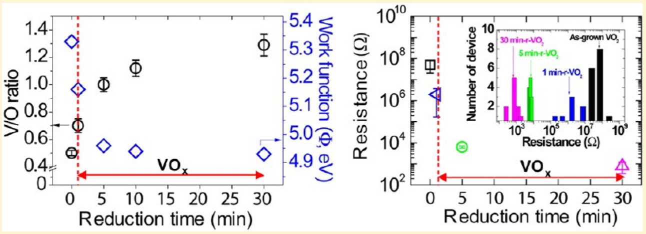

KEYWORDS: *Morphotropic transformation, vanadium dioxide, metal−insulator transition, hydrogen annealing, reduction, compositional variation*

Vanadium dioxide (VO_2) is a strongly correlated oxide exhibiting a first-order metal−insulator transition (MIT) that is accompanied by a structural phase transition from a low-temperature monoclinic phase to a high-temperature rutile phase.[1−3] Although the mechanism by which the MIT occurs in VO_2 is still being debated, the MIT in VO_2 is usually driven by strong electron−electron correlations associated with the Mott transition[4] or electron−phonon interactions associated with the Peierls transition.[5] VO_2 has attracted significant attention because of a variety of possible applications based on its ultrafast MIT.[6] Accordingly, many efforts have been made to understand the significant influences of stoichiometry,[7−10] interfacial stress,[11,12] external strain,[13−18] and doping[19−22] on the metal−insulator phase transition of VO_2.

For example, recently, Zhang et al have demonstrated the influence of stoichiometry on the phase transition from monoclinic to rutile structure in free-standing single-crystalline VO_2 nanobeams.[7] They showed that annealing of the nanobeams under vacuum conditions stabilized the rutile phase due to a deficiency of oxygen, suppressing the MIT as low as 103 K. In addition, a sputter deposition method using the variation of partial pressure of oxygen gas[8,9] to change the stoichiometry of vanadium oxide thin films has been announced. Son et al. have suggested that varying the reaction conditions in the low-temperature hydrothermal treatment of nanoscale VO_2 crystals could control the morphology and composition of the VO_2 micro- and nanocrystals.[10]

Noticeably, Natelson and co-workers[20,21] have demonstrated that hydrogen doping can be an effective method to control the electron carrier concentration, which results in the electronic phase transition (i.e., the Mott transition[4]) that occurs in this material. They showed that the MIT in single-crystalline VO_2 nanowires could be modulated by using electrochemical gating through electrochemical doping of the bulk of the VO_2 materials for hydrogen-containing ionic liquids.[20] They also

Received: February 8, 2013
Published: March 4, 2013

© 2013 American Chemical Society

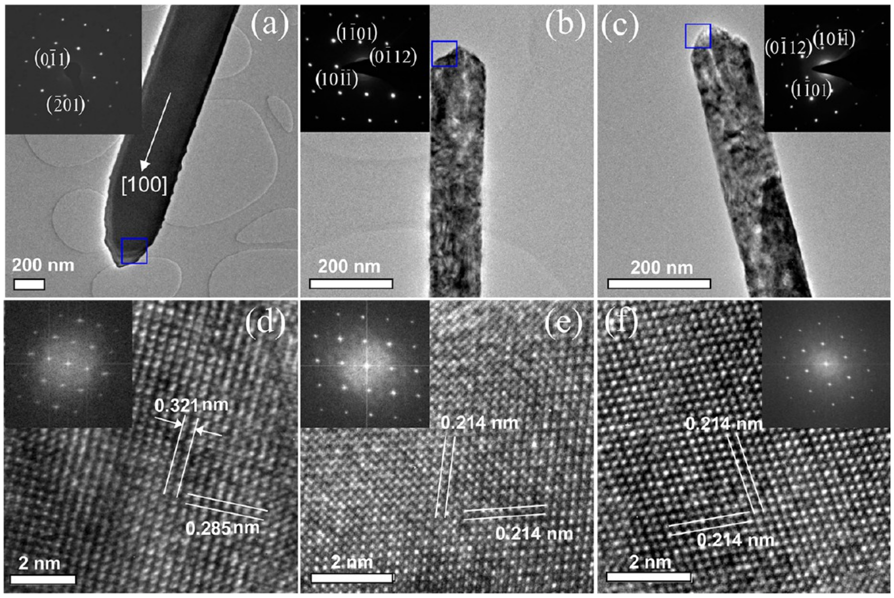

Figure 1. (a−c) Low-magnification bright-field TEM images of as-grown and reduced VO_2 nanobeams: (a) as-grown VO_2, (b) 1 min-r-VO_2, and (c) 30 min-r-VO_2 nanobeams. The corresponding SAED patterns are shown in the inset of each image. The zone axes are [122] and $[01\bar{1}1]$ for the as-grown and reduced VO_2 nanobeams, respectively. (d−f) HRTEM images obtained near the tips (marked by squares) of the VO_2 nanobeams. The FFT pattern of each HRTEM image is shown in the inset.

demonstrated that the MIT could be significantly modified by reversible doping with atomic hydrogen via low-temperature hydrogen annealing using the catalytic spillover method, accompanied by structural phase transition.[21] Furthermore, Sim et al. have suggested that the reversible resistance modulation using the liquid electrolyte can also be achieved by electrostatically driven carrier doping near VO_2 surface from the studies of comparing the ionic liquid gating and the hydrogen annealing of VO_2 films and membranes.[22]

Herein, we have demonstrated a morphotropic phase transformation (MPT) in single-crystalline VO_2 nanobeams caused by thermal reduction in a hydrogen environment using thorough experimental analyses that provide the correlation among structural phase transition, compositional variation, and electronic properties in VO_2 nanobeams. Unlike hydrogen doping method at moderate temperatures (100−200 °C),[21,22] hydrogen exposure at elevated temperatures (~400 °C) causes a reduction of the VO_2 nanobeams, resulting in compositional variations with distinctive reduction kinetics that depend on annealing time. The compositional variation leads to structural and electronic phase transitions, and a modification of the work function of VO_2 nanobeams. Specifically, the as-grown VO_2 nanobeam with a stoichiometric composition is monoclinic and insulating phases at room temperature with a relatively higher work function, whereas the reduced VO_2 nanobeam has a nonstoichiometric composition, and it is hexagonal-close-packed (hcp) and metallic phases over a large range of temperatures with a lower work function. Intriguingly, the work function and the electronic conductance of the nanobeams are correlated with the kinetics of the compositional variation. These properties can be explained by the formation of oxygen-deficiency-related defects in the nanobeam after the reduction. Our results will provide the comprehensive understanding of the phase transitions associated with the compositional variation for strongly correlated vanadium oxide systems.

All of the single-crystalline VO_2 nanobeams used in this study were grown on r-cut sapphire substrates using a vapor phase transport process, as described elswhere.[3] We used a high-pressure hydrogen annealing (HPHA) process to induce the morphotropic phase transition in the VO_2 nanobeams.[23] Specifically, the as-grown VO_2 nanobeams were annealed in 10 atm of H_2 at ~400 °C in a dedicated HPHA chamber. Different sets of nanobeams were reduced for 1, 5, 10, and 30 min and are denoted as 1 min-r-VO_2, 5 min-r-VO_2, 10 min-r-VO_2, and 30 min-r-VO_2 nanobeams, respectively. We investigated the MPT of the VO_2 nanobeams using transmission electron microscopy (TEM) that includes scanning transmission electron microscopy (STEM) and energy dispersive X-ray spectroscopy (EDS) capabilities (Technai G2 F30 S-Twin, FEI), ultraviolet photoemission spectroscopy (UPS) and X-ray photoemission spectroscopy (XPS) (AXIS-NOVA, Kratos, Inc.),[24] and Raman spectroscopy (NT-MDT, Russia).[25] The electronic transport characteristics were measured using a semiconductor characterization system (Keithley 4200) and surface potential measurements were carried out using atomic force microscopy (AFM, Nanoscope Multimode system, Veeco Instruments).

Panels a−c of Figure 1 show the bright-field TEM images of the as-grown VO_2, 1 min-r-VO_2, and 30 min-r-VO_2 nanobeams, respectively. The surface morphology of the as-grown VO_2 nanobeam (Figure 1a) is smooth, whereas those of the annealed VO_2 nanobeams (Figure 1b,c) are rough. The insets (the upper rows in Figure 1) are the corresponding selected area electron diffraction (SAED) patterns of the images for the VO_2 nanobeams. The SAED pattern of the as-grown VO_2 nanobeam (the inset of Figure 1a), taken along the [122] zone axis, indicates a single-crystalline monoclinic structure with a [100] growth direction, whereas those of the annealed VO_2 nanobeams demonstrate that the nanobeams are single-crystalline hcp structures (or rhombohedral) at the zone axis of $[01\bar{1}1]$ with space group $R\bar{3}c$ (see Figure S1 in the Supporting Information that demonstrates the diffraction patterns of the reduced VO_2 nanobeams in other zone axes).[26]

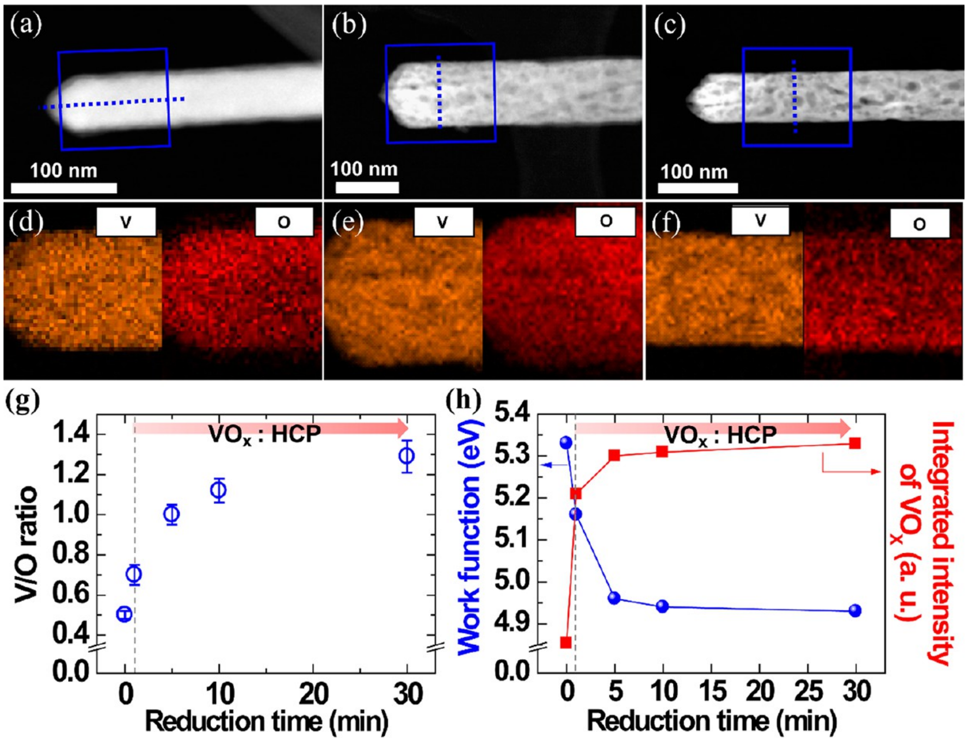

Figure 2. (a−c) HAADF STEM images of the VO_2 nanobeams shown in Figure 1a−c. (d−f) STEM EDS maps of the VO_2 nanobeams. (g) Change in V/O compositional ratio as a function of reduction time. (h) The integrated intensity of nonstoichiometric VO_x obtained from the XPS measurements for the VO_2 nanobeams and their corresponding work functions extracted from UPS measurements.

The HRTEM images acquired near the tips (indicated by squares in panels a−c of Figure 1) of the VO_2 nanobeams are shown in panels d−f of Figure 1. These confirm that the nanobeams are single-crystalline and demonstrate the structural transition from monoclinic structure to the hcp structure. For the as-grown VO_2 nanobeam (monoclinic structure), the lattice spacings of adjacent (011) and ($\bar{2}$01) planes are ~0.321 nm and ~0.285 nm, respectively (Figure 1d). On the other hand, for the annealed VO_2 nanobeams (hcp structure), the lattice spacings of neighboring ($\bar{1}$011) planes are ~0.214 nm, within our measurement accuracy of ~1% (Figure 1e,f). These measurements are in good agreement with the fast Fourier transformation (FFT) shown in the insets of panels d−f of Figure 1.

To quantify the surface morphology and compositional variation, we carried out STEM and EDS studies of the VO_2 nanobeams before and after hydrogen annealing. Panels a−c of Figure 2 show high-angle annular dark-field (HAADF) STEM images of the nanobeams, indicating that the surface roughening is more significant as the reduction time increases (see Figure S2 in the Supporting Information). The STEM EDS elemental line profiles obtained from the nanobeams demonstrate that the composition of vanadium (V) and oxygen (O) in each nanobeam is uniform following the dotted lines in the STEM images (see Figure S3 in the Supporting Information). The uniformity of the composition is confirmed by the STEM EDS maps (panels d−f of Figure 2), which were acquired from the regions marked by squares on the STEM images.

From the line-scan profiles, we determined V/O compositional ratios obtained from as-grown VO_2, 1 min-r-VO_2, 5 min-r-VO_2, 10 min-r-VO_2, and 30 min-r-VO_2 nanobeams, as summarized in Figure 2g. At each condition, we measured more than 10 VO_2 nanobeams to obtain averaged values of the composition. We found that there was a rapid increase in the V/O ratio as a function of annealing time, but this leveled off at a value of approximately V/O ≈ 1.3 Importantly, comparing these EDS data with analyses of the crystal structures discussed in Figure 1, it appears that the monoclinic structure is only stable at the stoichiometric composition near VO_2 at room temperature, whereas the hcp structure occurs over a wide range of the V/O ratio (approximately 0.7−1.3), similar to other oxide systems.[27,28] We note that this structure differs from one (i.e., orthorhombic or rutile structure) found in ref 21 where hydrogen doping was used to incorporate hydrogen atoms in the VO_2 nanobeams while maintaining their stoichiometry. We speculate that the unexpected hcp structure occurring by hydrogen annealing at high temperature (~400 °C) is related to the varied composition and the kinetics of reduction process. Such a broad range of nonstoichiometry can be attributed to the oxygen-deficiency-related defects such as vanadium interstitials and/or oxygen vacancies formed at the roughened surface of the nanobeams.[27,29−31] The oxygen-deficiency-related defects can act as crystallographic shear planes, indicating the lattice deformations by generating internal strain energy, leading to distinct compositions and structures.[7,30−32] We speculate that the formation of the defects may be the driving force to alter the composition and the crystalline structures of the vanadium oxide nanobeam.

The creation of the oxygen-deficiency-related defects also adjusts the oxidation state for charge neutrality in the nonstoichiometric surface, which strongly influences the work functions of materials.[9,29,33] The work function (Φ) is defined as the energy required to move an electron from Fermi energy level to the local vacuum energy level.[9,33] We measured the work function and the cation oxidation states of the nanobeams

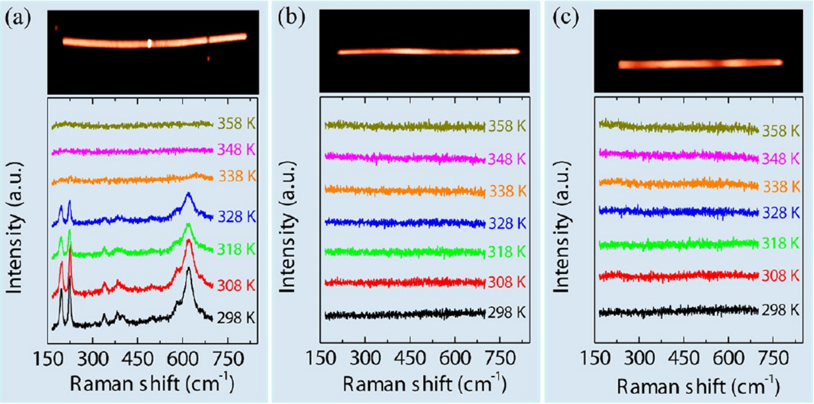

Figure 3. AFM topography images (upper row) acquired from (a) as-grown VO_2, (b) 1 min-r-VO_2, and (c) 30 min-r-VO_2 nanobeams, and their corresponding Raman spectra (lower row) acquired at different temperatures.

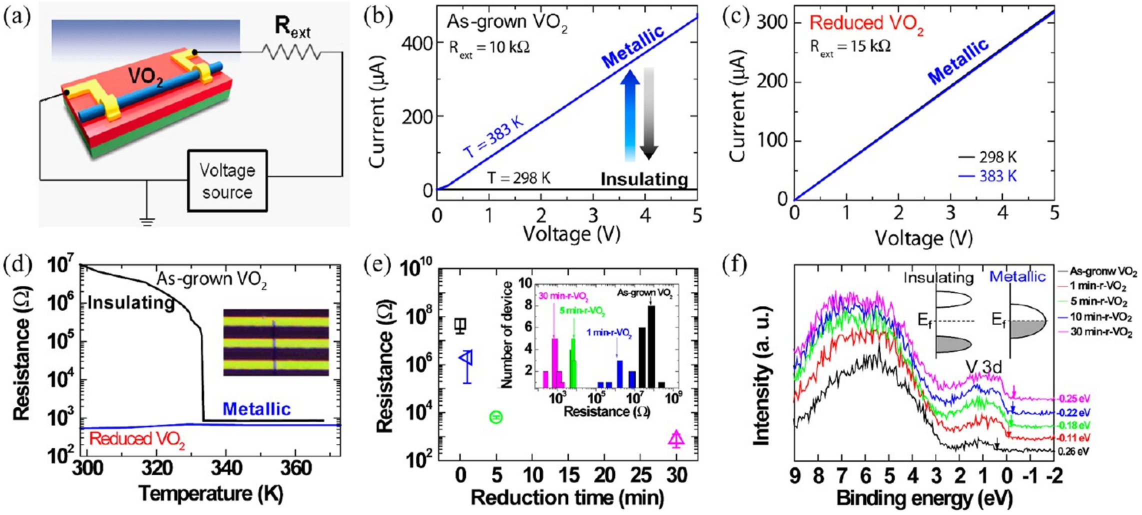

Figure 4. Electronic transport characteristics of two-terminal devices made from as-grown and reduced VO_2 nanobeams. (a) A schematic diagram of the VO_2 nanobeam device connected in series with external resistor (R_{ext}). (b,c) Electrical characteristics for (b) as-grown and (c) reduced VO_2 nanobeams at T = 298 and 383 K. (d) Temperature-dependence of the electrical resistance for the devices made from the as-grown and reduced VO_2 nanobeams. The inset shows the optical image of a two-terminal VO_2 nanobeam device. (e) Electrical resistance as a function of the reduction time for the as-grown and reduced VO_2 nanobeams. The inset shows statistical data of the electrical resistance at room temperature for as-grown VO_2, 1 min-r-VO_2, 5 min-r-VO_2, and 30 min-r-VO_2 nanobeams. (f) Valence band XPS spectra of the as-grown and reduced VO_2 nanobeams. The inset shows a schematic illustration displaying the DOS of insulating and metallic phases.

before and after the reduction using UPS and XPS.[24] Figure 2h shows the changes in the work functions and the integrated intensity of the fitted peaks related to nonstoichiometric compositions with lower cation oxidation states for the nanobeams (denoted as VO_x) as a function of the reduction time. The work function decreased steeply from 5.33 eV (before annealing: VO_2 (M)) to 4.96 eV (5 min annealing: VO (hcp)) and then its change rate slowed down as reduction time increased (see Figures S4a and S4b in the Supporting Information). Interestingly, this behavior tracks the trend of the V/O ratio (Figure 2g) in the VO_2 nanobeams before and after the reduction, indicating that only the intermediate range of the compositions between VO_2 and VO significantly affects the work function. From the V 2p core-level spectra of XPS, we explain that the increased intensity of the VO_x is attributed to the formation of the lower cation oxidation states due to the oxygen deficiency in the reduced VO_2 nanobeams (see Figure S5 in the Supporting Information). This result also shows that the formation of lower cation oxidation states has a dominating influence on the decrease of work function of the nanobeams after the reduction.[33] It should be noted that based on XPS data, the possibility of hydrogen doping in the course of the hydrogen annealing would not be considered (see Figure S6 in the Supporting Information).

To identify the electronic phase transformation of a single VO_2 nanobeam, we carried out the Raman measurements[25] at temperatures between 298 and 358 K. Figure 3 shows AFM topography images for individual VO_2 nanobeams and their corresponding Raman spectra at various temperatures (see Figure S7 in the Supporting Information). For the as-grown VO_2 nanobeam (Figure 3a), the vibration modes of Raman scattering in the monoclinic structure (insulating phase) are drastically different from those in the rutile structure (metallic phase), whic is in agreement with the data previously reported.[34−36] Interestingly, for the reduced VO_2 nanobeam (Figure 3b,c), Raman spectra measured at temperatures between 298 and 358 K show featureless scattering, indicating that the reduced VO_2 nanobeams are metallic phases. Combining the Raman data with the XPS data, we conclude

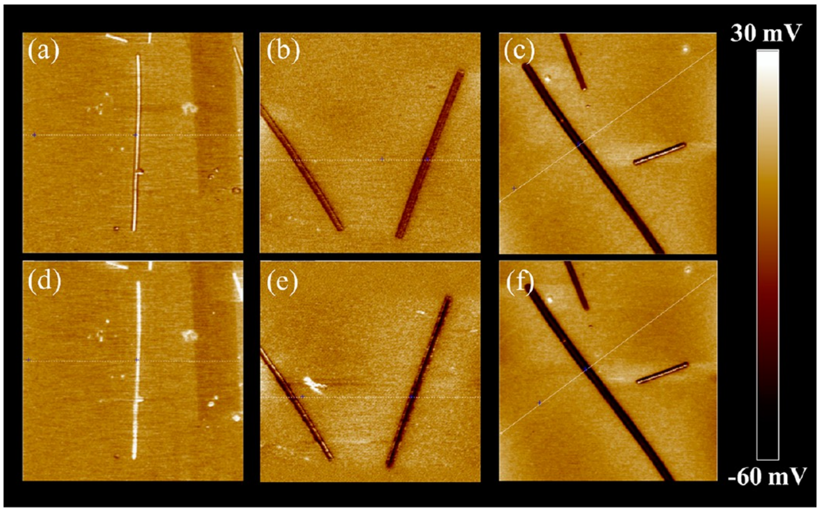

Figure 5. Surface potential maps corresponding to the same 20 × 20 μm^2 area for (a,d) as-grown VO_2, (b,e) 1 min-r-VO_2, and (c,f) 30 min-r-VO_2 nanobeams. The upper and lower panels show the surface potential maps at V_{tip} = 0 and 4 V, respectively.

that the metallicity of the reduced VO_2 nanobeams can be attributed to the presence of the mixed cation oxidation states.

To understand the correlation of the electronic properties with the structural and compositional variation, we examined the electronic transport characteristics of as-grown and reduced VO_2 nanobeams. By fabricating two-terminal devices, we measured the temperature-dependence of the electrical resistance for both types of nanobeams, as shown in panels a−e of Figure 4. As illustrated in Figure 4a, the two-terminal device fabricated with a VO_2 nanobeam lying on SiO_2 (100 nm) substrate was connected in series with an external resistor (R_{ext}) to limit the current flow during the phase transition of the nanobeam. The current versus voltage ($I-V$) characteristic for the as-grown VO_2 nanobeam indicates a phase transition from the insulating phase at T = 298 K to the metallic phase at T = 383 K, whereas for the reduced VO_2 nanobeam, it exhibits a metallic state at room temperature and over a large range of temperatures up to 383 K (Figure 4b,c). Figure 4d shows the temperature-dependence of electrical resistance for representative devices made from as-grown and reduced VO_2 nanobeams. For the as-grown VO_2 nanobeam, the electrical resistance starts from the insulating state at room temperature (T = 298 K) and then drops abruptly by a few orders of magnitude at the MIT temperature (T_{MIT} = 333 K). In contrast, the device made of the reduced VO_2 nanobeam exhibits markedly different resistance behavior, showing a stable metallic state over a large range of temperatures including room temperature (see Figure S8 in the Supporting Information).

Figure 4e shows the electrical resistance as a function of the reduction time. For these measurements, a total of 57 nanobeam devices were fabricated and characterized: 17 devices of as-grown VO_2, 7 devices of 1 min-r-VO_2, 23 devices of 5 min-r-VO_2, and 10 devices of 30 min-r-VO_2. The inset of Figure 4e presents statistical data for the electrical resistance at room temperature for as-grown, 1 min-r-VO_2, 5 min-r-VO_2, and 30 min-r-VO_2 nanobeams. We found that the electrical resistance decreased by a factor of $\sim 10^4$ for the 5 min-r-VO_2 nanobeam devices as compared with as-grown VO_2 nanobeam devices. In addition, the resistance of the 30 min-r-VO_2 nanobeam devices decreases by a factor of ~10 as compared with the 5 min-r-VO_2 nanobeam devices. Interestingly, the change in electrical resistance resembles the behaviors of the V/O ratio and the work function as a function of reduction time (Figure 2g,h).

Figure 4f presents the valence band XPS spectra of the as-grown and reduced VO_2 nanobeams. We found that the valence band maximum energy in the XPS spectra (marked by arrows) shifted toward the vacuum energy level. The edge of the valence band maximum energy for the as-grown VO_2 nanobeams was 0.28 eV, whereas that for the 1 min-r-VO_2, 5 min-r-VO_2, 10 min-r-VO_2, and 30 min-r-VO_2 nanobeams was −0.11, −0.18, −0.22, and −0.26 eV, respectively. These results indicate that for the reduced VO_2 nanobeam, the density of states (DOS) is enhanced in the vicinity of the Fermi energy level, which is a signature of metallic phase, as illustrated in the inset of Figure 4f.[37−39] The changes in density and distribution of electronic states provide substantial evidence that the formation of oxygen-deficiency-related defects can yield defect states and/or band-tail states within an energy gap, similar to other oxide systems.[33,40−42] This is also well supported by the valence band UPS data of the nanobeams (see Figure S4 in the Supporting Information). Therefore, we think that the change in electrical resistance by differing the annealing time would be attributed to the presence of the oxygen-deficiency-related defects at the nanobeam surfaces, the identical origin for the composition and work function mentioned above.

To further clarify the correlation between the surface properties and the electronic behaviors of the nanobeams, we also examined the surface potential (V_S) of the nanobeams before and after reduction (see Figures S9−S12 in the Supporting Information). Figure 5 shows images of the V_S at tip biases of 0 (the upper rows) and 4 V (the lower rows) for the as-grown VO_2 (Figure 5a,d), 1 min-r-VO_2 (Figure 5b,e), and 30 min-r-VO_2 nanobeams (Figure 5c,f) (also see Figure S11 in the Supporting Information). Interestingly, the V_S for the reduced VO_2 nanobeams exhibited completely different images compared with those for the as-grown VO_2 nanobeams, as shown in Figure 5. The observed surface potentials of the VO_2 nanobeams did not exhibit any noticeable tip-bias-dependent variations (see Figure S12 in the Supporting Information). Notably, the V_S for the as-grown VO_2 nanobeam was higher values than the background (Au substrate) V_S, leading to bright contrast images. This indicates that the as-grown VO_2 nanobeam contains a relatively higher work function. In contrast, the V_S of the reduced VO_2 nanobeams forms a dark contrast image because it is lower than the background V_S. This indicates that the reduced nanobeam has a smaller work function. We note that the observed surface potentials of the VO_2 nanobeams do not cause any noticeable tip-bias-dependent variations (see Figure S12 in the Supporting Information). The different contrast of the V_S between the as-grown and reduced VO_2 nanobeams is likely due to the compositional variation in the nanobeam, originating from the creation of the oxygen-deficiency-related defects on the surface of nanobeam.[9] This is also in a good agreement with the measurements of work function extracted from the UPS measurements (Figure 2 and Supporting Information Figure S4).

In summary, we have demonstrated the morphotropic phase transformation of single-crystalline VO_2 nanobeams, resulting from the thermal reduction in a hydrogen environment. We have observed a strong correlation among a structural phase transformation, compositional variations, and the modulations of electronic properties. The as-grown VO_2 nanobeam with stoichiometric composition has a monoclinic structure, a higher work function, and exhibit a metal−insulator transition. In contrast, the reduced VO_2 nanobeams have a nonstoichiometric composition and a lower work function, exhibit a hexagonal-close-packed structure, and are in the metallic state over a large range temperature. All of the composition, work function, and electrical conductance behaviors of the VO_2 nanobeams follow an identical trend with reduction time. These properties can be correlated to the creation of the oxygen-deficiency-related defects (i.e., interstitials and/or vacancies) formed in the VO_2 nanobeams during the reduction process. Our study will enhance the understanding of the complex phase transitions of vanadium oxides and thereby will provide a foundation for engineering diverse and desirable properties for a wide range of technological applications.

■ ASSOCIATED CONTENT

Ⓢ Supporting Information

EDS line profiles, UPS and XPS data, AFM topography images, and surface potential profiles for the as-grown and reduced VO_2 nanobeams. TEM analyses for a 5 min-r-VO_2 nanobeam, Raman spectra and surface potential maps for a 10 min-r-VO_2 nanobeam, surface potential measurement system using AFM. This material is available free of charge via the Internet at http://pubs.acs.org.

■ AUTHOR INFORMATION

Corresponding Author

*E-mail: (W.-K.H) wkh27@kbsi.re.kr; (B.J.K) kimbj@gist.ac.kr; (T.L) tlee@snu.ac.kr.

Present Address

¶(J.I.S.) Department of Engineering Science, University of Oxford, Oxford OX1 3PJ, United Kingdom.

Author Contributions

□W.-K.H. and J.-B.P. contributed equally.

Notes

The authors declare no competing financial interest.

■ ACKNOWLEDGMENTS

W.-K.H acknowledges the financial support from KBSI Grant T32516. B.J.K acknowledges the support from the Research Institute for Solar and Sustainable Energies (RISE) at Gwangju Institute of Science and Technology (GIST). T.L acknowledges the support from the National Creative Research Laboratory program (Grant 2012026372) by the Korean Ministry of Education, Science, and Technology.

■ ABBREVIATIONS

MPT, morphotropic phase transformation; MIT, metal−insulator transition; SPT, structural phase transition; HPHA, high pressure hydrogen annealing; hcp, hexagonal close-packed; XPS, X-ray photoemission spcectroscopy; UPS, ultraviolet photoemission spectroscopy; SAED, selected area electron diffraction; STEM, scanning transmission electron microscopy; EDS, energy dispersive X-ray spectroscopy; HAADF, high-angle annular dark-field; DOS, density of states; AFM, atomic force microscope

■ REFERENCES

(1) Zylbersztejn, A.; Mott, N. F. *Phys. Rev. B* **1975**, *11*, 4383−4395.

(2) Morin, F. J. *Phys. Rev. Lett.* **1959**, *3*, 34−36.

(3) Sohn, J. I.; Joo, H. J.; Porter, A. E.; Choi, C. −J.; Kim, K.; Kang, D. J.; Welland, M. E. *Nano Lett.* **2007**, *7*, 1570−1574.

(4) Qazilbash, M. M.; Brehm, M.; Chae, B. −G.; Ho, P. -C.; Andreev, G. O.; Kim, B. −J.; Yun, S. J.; Balatsky, A. V.; Maple, M. B.; Keilmann, F.; Kim, H. −T.; Basov, D. N. *Science* **2007**, *318*, 1750−1753.

(5) Wentxcovitch, R. M.; Schulz, W. W.; Allen, P. B. *Phys. Rev. Lett.* **1994**, *72*, 3389.

(6) Yang, Z.; Ko, C.; Ramanathan, S. *Annu. Rev. Mater. Res.* **2011**, *41*, 337−367.

(7) Zhang, S.; Kim, I. S.; Lauhon, L. J. *Nano Lett.* **2011**, *11*, 1443−1447.

(8) Griffiths, C. H.; Eastwood, H. K. *J. Appl. Phys.* **1974**, *45*, 2201−2206.

(9) Ko, C.; Yang, Z.; Ramanathan, S. *ACS Appl. Mater. Interfaces* **2011**, *3*, 3396−3401.

(10) Son, J. −H.; Wei, J.; Cobden, D.; Cao, G.; Xia, Y. *Chem. Mater.* **2010**, *22*, 3043−3050.

(11) Wu, J.; Gu, Q.; Guiton, B. S.; de Leon, N. P.; Ouyang, L.; Park, H. *Nano Lett.* **2006**, *6*, 2313−2317.

(12) Sohn, J. I.; Joo, H. J.; Kim, K. S.; Yang, H. W.; Jang, A. −R.; Ahn, D.; Lee, H. H.; Cha, S.; Kang, D. J.; Kim, J. M.; Welland, M. E. *Nanotechnology* **2012**, *23*, 205707.

(13) Cao, J.; Ertekin, E.; Srinivasan, V.; Fan, W.; Huang, S.; Zheng, H.; Yim, J. W. L.; Khanal, D. R.; Ogletree, D. F.; Grossman, J. C.; Wu, J. *Nat. Nanotechnol.* **2009**, *4*, 732−737.

(14) Guo, H.; Chen, K.; Oh, Y.; Wang, K.; Dejoie, C.; Syed Asif, S. A.; Warren, O. L.; Shan, Z. W.; Wu, J.; Minor, A. M. *Nano Lett.* **2011**, *11*, 3207−3213.

(15) Hu, B.; Ding, Y.; Chen, W.; Kulkarni, D.; Shen, Y.; Tsukruk, V. V.; Wang, Z. L. *Adv. Mater.* **2010**, *22*, 5134−5139.

(16) Hu, B.; Zhang, Y.; Chen, W.; Xu, C.; Wang, Z. L. *Adv. Mater.* **2011**, *23*, 3536−3541.

(17) Atkin, J. M.; Berweger, S.; Chavez, E. K.; Raschke, M. B.; Cao, J.; Fan, W.; Wu, J. *Phys. Rev. B* **2012**, *85*, 020101(R).

(18) Tselev, A.; Strelcov, E.; Luk'yanchuk, I. A.; Budai, J. D.; Tischler, J. Z.; Ivanov, I. N.; Jones, K.; Proksch, R.; Kalinin, S. V.; Kolmakov, A. *Nano Lett.* **2010**, *10*, 2003−2011.

(19) Wu, C.; Feng, F.; Feng, J.; Dai, J.; Peng, L.; Zhao, J.; Yang, J.; Si, C.; Wu, Z.; Xie, Y. *J. Am. Chem. Soc.* **2011**, *133*, 13798−13801.

(20) Ji, H.; Wei, J.; Natelson, D. *Nano Lett.* **2012**, *12*, 2988−2992.

(21) Wei, J.; Ji, H.; Guo, W.; Nevidomskyy, A. H.; Natelson, D. *Nat. Nanotechnol.* **2012**, *7*, 357−362.

(22) Sim, J. S.; Zhou, Y.; Ramanathan, S. *Nanoscale* **2012**, *4*, 7056−7062.

(23) Yoon, J.; Hong, W. −K.; Jo, M.; Jo, G.; Choe, M.; Park, W.; Sohn, J. I.; Nedic, S.; Hwang, H.; Welland, M. E.; Lee, T. *ACS Nano* **2011**, *5*, 558−564.

(24) The work function of all the samples was obtained from ultraviolet photoelectron spectroscopy (UPS, AXISNOVA, Kratos, Inc.) (He I, *hv* = 21.22 eV). The pass energy of the analyzer was 5 eV. In addition, X-ray photoelectron spectroscopy (XPS) measurements were carried out using AXIS-NOVA spectrophotometer equipped with a monochromatic Al K-alpha X-ray source (1486.6 eV) (Kratos, Inc.). The pass energy of the analyzer was 40 eV and the spot size of X-ray beams was 1 mm × 2 mm.

(25) Raman spectra were measured by using a Cobolt Blues laser (Cobolt, Sweden) operating at a wavelength of ~473 nm in an NTEGRA Spectra spectrometer (NT-MDT, Russia) with a spectral resolution of 0.7 cm^{-1}. The laser beam was focused and the Raman signals were collected by 100× objective (NA = 0.7). The laser power was ~0.3 mW at the focused-beam spot with a diameter of ~412 nm. The Raman signals were detected by Newton EMCCD array detector and NT-MDT Nova software was used for data acquisition and control.

(26) Finger, L. W.; Hazen, R. M. *J. Appl. Phys. Lett.* **1980**, *51*, 5632.

(27) Gélard, I.; Jehanathan, N.; Roussel, H.; Gariglio, S.; Lebedev, O. I.; Tendeloo, G. V.; Dubourdieu, C. *Chem. Mater.* **2011**, *23*, 1232−1238.

(28) Solonin, Y. M.; Khyzhun, O. Y.; Graivoronskaya, E. A. *Cryst. Growth Des.* **2001**, *1*, 473−477.

(29) Gopalakrishnan, J.; Rao, C. N. R. *New Directions in Solid State Chemistry*; Cambridge University Press: New York, 1997.

(30) Zakrzewska, K. *Adv. Mater. Sci. Eng.* **2012**, DOI: 10.1155/2012/826873.

(31) Reece, M.; Morrell, R. *J. Mater. Sci.* **1991**, *26*, 5566−5574.

(32) Katzke, H.; Schlögl, R. *Acta Crystallogr.* **2003**, *B59*, 456−462.

(33) Greiner, M. T.; Chai, L.; Helander, M. G.; Tang, W. −M.; Lu, Z. −H. *Adv. Funct. Mater.* **2012**, *22*, 4557−4568.

(34) Pan, M.; Liu, J.; Zhong, H.; Wang, S.; Li, Z. −f.; Chen, X.; Lu, W. *J. Cryst. Growth* **2004**, *268*, 178−183.

(35) Chou, J. Y.; Lensch-Falk, J. L.; Hemesath, E. R.; Lauhon, L. J. *J. Appl. Phys.* **2009**, *105*, 034310.

(36) The monoclinic (M) structure showed Raman peaks at 195 (A_g), 225 (A_g), 258 (B_g), 308 (A_g), 339 (B_g), 392 (A_g), 396 (B_g), 453 (B_g), 489 (B_g), 585 (A_g), and 620 cm^{-1} (A_g), whereas the rutile (R) structure showed a broad band between 200 and 700 cm^{-1}.

(37) Burkhardt, W.; Christmann, T.; Meyer, B. K.; Niessner, W.; Schalch, D.; Scharmann, A. *Thin Solid Films* **1999**, *345*, 229−235.

(38) Burkhardt, W.; Christmann, T.; Franke, S.; Kriegseis, W.; Meister, D.; Meyer, B. K.; Niessner, W.; Schalch, D.; Scharmann, A. *Thin Solid Films* **2002**, *402*, 226−231.

(39) Shin, S.; Suga, S.; Taniquchi, M.; Fujisawa, M.; Kanzaki, H.; Fujimori, A.; Daimon, H.; Ueda, Y.; Kosuge, K.; Kachi, S. *Phys. Rev. B* **1990**, *43*, 4993−5009.

(40) Diebold, U. *Surf. Sci. Rep.* **2003**, *48*, 53−229.

(41) Stausholm-Møller, J.; Kristoffersen, H. H.; Hinnemann, B.; Madsen, G. K. H.; Hammer, B. *J. Chem. Phys.* **2010**, *133*, 144708.

(42) Chen, X.; Liu, L.; Yu, P. Y.; Mao, S. S. *Science* **2011**, *331*, 746−749.